Palaeogeography, Palaeoclimatology, Palaeoecology 596 (2022) 110973

Contents lists available at ScienceDirect

Palaeogeography, Palaeoclimatology, Palaeoecology

journal homepage: www.elsevier.com/locate/palaeo

Astronomically forced cycles in Middle Permian fluvial sediments from Karoo Basin (South Africa)

L. Lanci [a,*], S. Galeotti [a], K. Ratcliffe [b], E. Tohver [c], A. Wilson [d,e], S. Flint [d]

[a] Department of Pure and Applied Science, University of Urbino, "Carlo Bo", Via Ca' Le Suore 2, I-61029 Urbino (PU), Italy
[b] Chemostrat Ltd., Unit 1 Ravenscroft Court, Welshpool, Powys SY21 9BW, United Kingdom
[c] Institute of Astronomy, Geophysics and Atmospheric Sciences, University of São Paulo, Rua do Matão, 1226 São Paulo, Brazil
[d] Department of Earth and Environmental Sciences, University of Manchester, United Kingdom
[e] ImageStrat Pty Ltd, 1131 Hay Street, West Perth 6005, Western Australia, Australia

ARTICLE INFO

Editor: Howard Falcon-Lang

Keywords:
Cyclostratigraphy
Fluvial sediments
Magnetic stratigraphy
Kiaman superchron
Geochronology
Major element oxides

ABSTRACT

We report evidence for Milankovitch cycles discovered in Middle Permian strata of the fluvial Abrahamskraal formation, lower Beaufort Group, in Karoo Basin of the Northern Cape Province, South Africa. Statistical analyses of ranked lithologies and of major element oxides have been used to obtain clusters of elements that capture lithological variations and reflect changes of the sedimentary environment through time. Spectral analysis of these elemental statistical groups reveal significant meter-scale sedimentary cycles of 67 m, 17.5 m, 5.9 m and 3.5–2.8 m, which can be interpreted as the sedimentary expression of astronomical forcing, based on the available estimate of sedimentation rate. The identified periods of short-eccentricity, precession and obliquity show a good match with those predicted for Middle Permian times, providing a data-based validation of the astronomical theory. Cycle counting integrated with available U—Pb dating, provides a cyclochronological calibration for Wordian normal magnetozones and, combined with radiometric ages, indicates an age of 266.5 ± 0.26 Ma for the end of Kiaman superchron. Recognition of the orbitally driven sedimentation in Gondwana supercontinent suggest a global extension of astronomical influence of Permian climate and confirms empirical knowledge of Earth's astronomical parameters before 260 million years ago. The new data demonstrate a rare case of astronomically paced cyclicity in fluvial deposits and a unique cyclostratigraphic record of the Middle Permian Gondwana supercontinent whose sedimentation reflects orbitally-paced precipitation changes.

1. Introduction

Tectonics, eustatic sea-level changes, autocyclic processes and environment forcing are the driving mechanisms in the formation of depositional sequences. Among these controlling factors, the astronomical forcing by Milankovitch cycles are of particular interest as they are predictable. Because it can provide a temporal framework for a sedimentary sequence and a direct link to Earth's climate fluctuations through insolation variability. In the Permian period, the study of astronomical rhythms from the stratigraphic record is challenging because of inherent limitations of astronomical solutions and the chaotic nature of solar system motion. However, cyclic sedimentation controlled by changes in the Earth's orbit during the Middle Permian have been reported and related to climate fluctuations resulting from growth and waning of Late Paleozoic ice-sheets. For example, recent cyclostratigraphic studies in Permian marine sequences from southern China confirmed the presence of Milankovitch cycles recorded in the Middle to Late Permian sediments (Wu et al., 2013; Yao et al., 2015; Fang et al., 2015, 2017; Cong et al., 2019; Yao and Hinnov, 2019). The imprint of Milankovitch cycles in South China, Gufeng Formation of Roadian-Capitanian age, which is characterized by rhythmic chert–mudstone couplets deposited on a continental shelf, has been reported by Yao et al. (2015). Cong et al. (2019) recognized astronomically forced parasequences controlled by sea-level changes in the Middle Permian Maokou Formation (China) suggesting the presence of orbitally-driven glacio-eustasy. Continental sedimentary successions are sparse but they can provide high-resolution paleoclimate archives and offer information of orbitally forced climate change and depositional system responses on land records. Cyclostratigraphic study of continental sequences in the Middle Permian lacustrine sediments in

* Corresponding author.
E-mail address: luca.lanci@uniurb.it (L. Lanci).

https://doi.org/10.1016/j.palaeo.2022.110973
Received 28 January 2022; Received in revised form 29 March 2022; Accepted 30 March 2022
Available online 4 April 2022

northwestern China was reported by Huang et al. (2020) but no coheval records are available for the Southern hemisphere. Fluvial sediments of the Abrahamskraal Formation (Beaufort Group) in the Karoo Basin of South Africa were deposited on the southwestern part of Gondwana supercontinent with paleomagnetic data indicating a paleolatitude of ca. 47° S (Lanci et al., 2013). They represent a unique record of fluvial deposition corroborated by radiometric dating and magnetostratigraphic data. This paper investigates the variability of the Middle Permian Karoo sediment deposition on the Milankovitch time-scales starting from the robust time frame, which constitutes the basis for cyclostratigraphy, provided by previous radiometric and magnetostratigraphic studies on the same site (Lanci et al., 2013; Tohver et al., 2015) and the underlying Ecca Group (Belica et al., 2017).

2. Geologic and stratigraphic setting

The sediments of the Karoo Basin record a long history of sedimentation straddling the Paleozoic to middle Mesozoic, accumulating up to 5500 m of sediments in thickness (Tankard et al., 2009). The base of the Karoo supergroup is defined by the glaciogenic diamictites of the Dwyka Group, which represents a sedimentary record of the Permo-Carboniferous glaciation of the southern Gondwana, laying over a ca.30 Myr stratigraphic hiatus. The turbidites and deltaic sandstones and mudstones of the Ecca Group, deposited during the Kiaman Reversed Superchron (Belica et al., 2017), overlying the Dwyka group. They capture the transition to a deep-water depositional setting, following the postglacial sea-level rise. The transition to a continental setting is inferred from the deposition of the fluvial sediments of the Adelaide Subgroup and of the lowermost Beaufort Group. These represent typical meandering river systems, with fine grained mud- and siltstones beds, 1–5 m thick, interbedded with coarser grained, 5–10 m thick channel fill fine-grained sandstones, which are the target of this study. In the study area the sedimentation of the Beaufort Group is interrupted in the middle Triassic by a stratigraphic hiatus. Overall, the Karoo Basin sedimentation terminated during the Jurassic (ca. 180 Ma) as a consequence of the extensional tectonics that resulted in the emplacement of continental flood basalts with concomitant dyke and sill intrusions (Tankard et al., 2009).

The sediments of the Karoo Basin accumulated under the influence of two main allogenic controls, tectonism and climate. On the ten million year time scale, the lithostratigraphic succession of the Karoo Supergroup reflects a basin fill episode from the glaciomarine Dwyka Group at its base, followed by turbidites through marine-deltaic deposits of the Ecca Group, to the fluvial Beaufort Group that outcrops at Ouberg Pass in the Northern Cape and represents the first continental strata. In its lower part, which in the western part of the basin (Adelaide Subgroup) includes the Abrahamskraal Fm., the transition to a continental setting is inferred from the fluvial sediments with fine grained mud- and siltstone beds, 0.04–7.00 m thick, interbedded with coarser grained, 0.5–19.8 m thick channel-fills (Catuneanu et al., 2005; Wilson et al., 2014; Gulliford et al., 2014; Bordy and Paiva, 2021, and references therein). The stratigraphic record of the Karoo Supergroup shows evidence of a general shift from cold and semi-arid conditions during the Late Carboniferous–earliest Permian interval, to warmer and eventually hot climates with fluctuating precipitation during the end-Paleozoic to early Mesozoic times (Keyser, 1966; Visser and Dukas, 1979; Stavrakis, 1980; Tankard et al., 1982; Visser, 1991a, 1991b). During deposition of the Beaufort Group, the climate had warmed sufficiently to become semi-arid with seasonally-controlled rainfall (Smith, 1990).

On shorter time scales, Bordy and Paiva (2021) suggested that the upper member (Capitanian age) of the Abrahamskraal Fm. was subject to a basinwide allogenic control thought climate changes, but overall the influence of climate variability in the interior of Gondwana supercontinent is mostly unknown.

3. Data and methods

3.1. Location and sampling

The studied section is located at Ouberg Pass (S 32° 24.44′, E 20° 19.58′) along the gravel road that descends the Great Escarpment, west of the town of Sutherland (Fig. 1). The outcropping lithologies encompass the uppermost Waterford Fm., which defines the top of the Ecca Group, and the lower ca. 413 m of the Abrahamskraal Fm. that belongs to the Lower Beaufort Group, for a total exposure thickness of about 540 m. The base of the Abrahamskraal Fm. was conventionally set at the 98 m mark in our stratigraphic profile (Lanci et al., 2013) at the first appearance of red mudstones according to the criteria of Rossouw and De Villers (1953) although the transition between the formations is gradual. In this study we restrict the analysis to the Abrahamskraal Fm. because of the availability of ash beds yielding radiometric dates and the presence of geomagnetic reversals (reported in Lanci et al., 2013). Moreover, the underlying Waterford Fm. has different lithologies, reflecting different sedimentary processes and sedimentation rates.

In the field, the samples lithology was described and about 20 g of sediments were taken at intervals of ca. 0.5 m, avoiding as much as possible superficial weathering (Ratcliffe et al., 2015). A total of 766 samples are analysed in this study. In the laboratory, an aliquot of approximately 5 g was taken from each sample and ground to a fine powder using a planetary ball mill. From that aliquot, subsamples weighing ca. 0.25 g were prepared using a $LiBO_2$ fusion (Jarvis and Jarvis, 1992a, 1992b). The resultant solutions were analysed by inductively coupled plasma optical emission spectrometry and mass spectrometry (ICP OES-MS) resulting in data being acquired for major element oxides SiO_2, Al_2O_3, TiO_2, Fe_2O_3, MnO, MgO, CaO, Na_2O, K_2O and P_2O_5. The analytical instruments are calibrated using certificated rock standards, with instrument drift being monitored after every five samples and, if necessary, corrected by the instrument software. Precision error for the major-element oxides is below 2%. Methodological details are described in Ratcliffe et al. (2015).

3.2. Geochronological setting and expected astronomical periods

The Abrahamskraal Fm. at Ouberg Pass was studied for magnetic stratigraphy and radiometric dating by Lanci et al. (2013) who reported a U/Pb age from ca. 264.6 Ma near the top of the section to 268.5 Ma near the boundary with the underlying Waterford Fm. A subsequent study of McKay et al. (2015) confirmed the radiometric age of the Ouberg Pass section and recent U—Pb zircon age constraints on the middle and upper part of the Abrahamskraal Fm. (Day et al., 2022) indirectly corroborated the results of Lanci et al. (2013). Magnetostratigraphy identified the top of the Kiaman reversed superchron at Ouberg Pass and extended the polarity sequence in stratigraphically correlated sections (Lanci et al., 2013; Tohver et al., 2015). U/Pb radiometrically dated levels provide a first order estimate of the averaged sedimentation rate, which is obtained as the slope of the best-fit regression line, weighted for inverse of analytic errors, of five levels located in the top 400 m of the section, approximately the same section studied for cyclostratigraphy. The slope of the regression line is −8.98 kyr/m with a large uncertainty (σ = 2.09 kyr/m) which is shown in Fig. S1 as a grey band that represents the 95% confidence limit for the best-fit line. The negative sign is due to the stratigraphic thickness increasing up-section and corresponds to a sedimentation rate of about $1/8.98 \times 100 = 11.1$ cm/kyr.

Cyclostratigraphy relies on correct matching of observed sedimentary cycles to predicted astronomical periodicities, in particular eccentricity, obliquity, and equinox precession. These periodicities, however, varied in the past and their calculation is subject to the uncertainty of recession history of the Moon's orbit and tidal dissipation, which are not well constrained. Changes are expected to have affected mostly the precession and obliquity periodicities while eccentricity is unlikely to

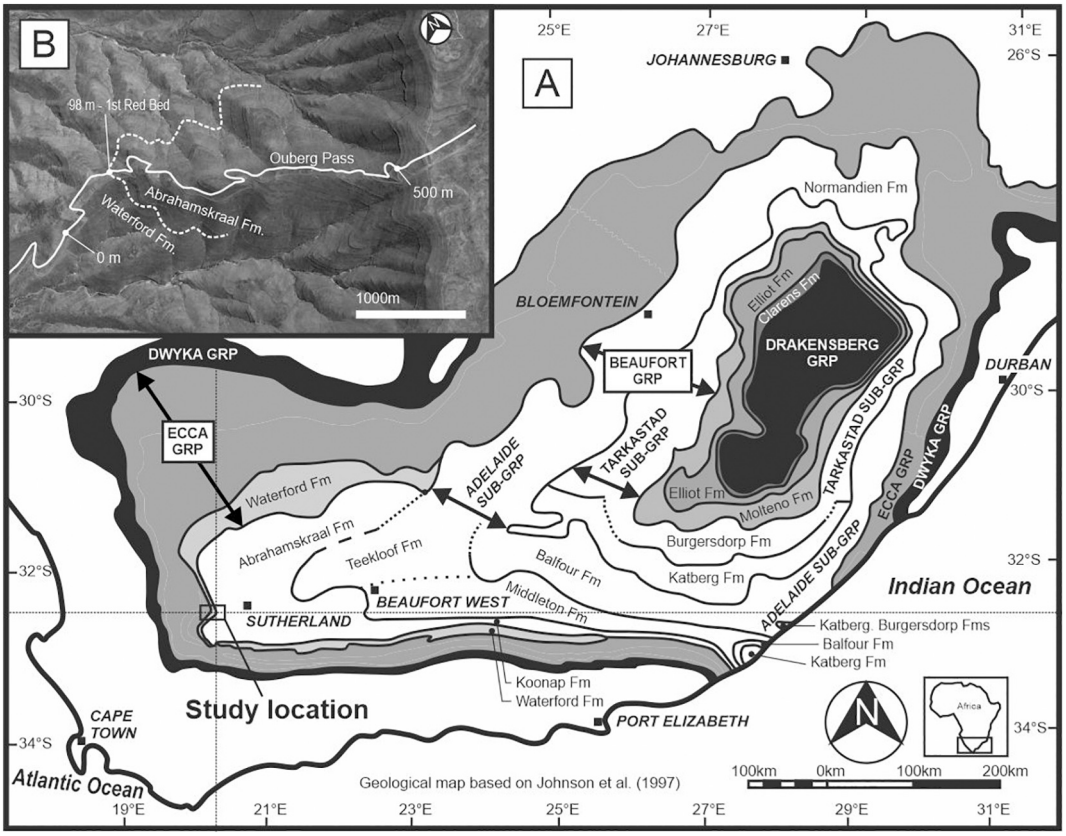

Fig. 1. A) Sketch geological map redrawn from Johnson et al. (1997) and B) map of the studied area.

have varied greatly. We have estimated the expected astronomical periods for the Middle Permian according to Waltham's (2015) tidal dissipation model using the on-line calculator http://nm2.rhul.ac.uk/Milankovitch1.html for an age of 260 Ma (Table S1). These values are not significantly different from those computed according to the calculations of Laskar et al. (2004), which can be found in the supplemental material, and match well the power spectral peaks found in the Middle Permian sediments of the lacustrine Lucaogou Formation, China (Huang et al., 2020).

3.3. Data and spectral analysis

The major element oxide concentrations constitute a multivariate dataset describing the chemistry of sediment composition. We found that the concentrations of major element oxide at Ouberg Pass are highly correlated to each other suggesting that they represent a limited number of lithotypes. Therefore, we have reduced them to a single and statistically more robust parameter, representing the abundance of a correlated groups of oxides that can also be related to specific lithotypes. This dimensionality reduction was achieved by principal component analysis (PCA) computing the eigenvalues of the covariance matrix and projecting each data point onto the major eigenvector(s) that represent the majority of the data variance (e.g., Jolliffe and Cadima, 2016).

Power spectra were computed by the smoothed Lomb-Scargle periodogram (Lomb, 1976; Scargle, 1982) which was used to estimate the spectral power on the original data which are irregularly spaced because of some sampling gaps. Periodogram smoothing was simply achieved using a 5 point running average. More sophisticated spectral analysis was performed on the numerical series after resampling the data to an evenly spaced interval of 0.5 m by linear interpolation. Spectral analysis of the interpolated record included the calculation of power spectrum that was performed using the multi-taper method (MTM) (Thomson, 1982) and significance levels estimated rejecting the null auto-regressive model of first order according to Mann and Lees (1996). Power spectra were computed with three 2π tapers corresponding to a resolution bandwidth of 0.0192 m^{-1} at the given sampling interval. Wavelet power spectra and cumulative spectra with confidence level were computed according to the method of Torrence and Compo (1998) and subsequent corrections (Liu et al., 2007), using a Morlet wavelet with a characteristic frequency of seven. Amplitudes are scaled with the variance of the respective index; hence, the expected power of white noise is 1. Frequency modulation (FM) of the filtered components were used to identify the phase of the modulating forcing. Systematic shifts in astronomical frequencies of orbital components are described as FM patterns by Laurin et al. (2016). FM defines positive and negative interference patterns of orbital frequencies in wavelength components of evolutive harmonic analysis (EHA) (Rial, 1999; Meyers et al., 2001; Laurin et al., 2016). Negative interference of FM is associated with bifurcations of wavelength components, which indicates minimal conditions of the modulator—i.e., bifurcations of precession components reveal short eccentricity minima (Laurin et al., 2016). In contrast, positive interference of FM, which is identified by junctions of wavelength components, suggests maxima in the modulator—i.e., junctions of precession components reveal short eccentricity maxima. FM is resistant to simple sedimentary distortions, including 20–100% sedimentation-rate changes that are positively or negatively proportional to the precessional and eccentricity forcing (Laurin et al., 2016). Indeed, the detection of FM has been successfully applied to sedimentary intervals characterized by unclear amplitude modulation and remarkable shift in sedimentation rate (e.g. Galeotti et al., 2017).

All calculations were made using the freely available R program (R Core Team, 2015) with the packages "astrochron" (Meyers, 2014) and "biwavelet" (Gouhier et al., 2021). Calculations are available as a R-Studio notebook (https://www.rstudio.com) in the Supplemental material. The sedimentary cycles were tuned to the expected astronomical frequencies for the Middle Permian (Table S1) using the averaged

spectral misfit analysis that provided the optimal average sedimentation rate (Meyers and Sageman, 2007; Meyers, 2012). Additionally, the orbital components were extracted from the stratigraphic series to assess amplitude modulation using bandpass frequency filters.

4. Results and discussion

4.1. Data reduction of major element oxides

We find that several major element oxide concentrations (Fig. 3A) are higly correlated variables. Fig. 4A shows the Pearson's correlation coefficients between the single variables and shows that the data set can be divided into 3 strongly correlated groups, group 1 consisting of SiO_2 and Na_2O, group 2 consisting of TiO_2, Al_2O_3, K_2O, Fe_2O_3, and MgO, and group 3 composed of MnO and CaO. The concentration of MnO, CaO and P_2O_5 is negligible (below 2%, on average) therefore only groups 1 and 2 are indicative of the main mineralogical types constituting the Abrahamskraal Fm. Moreover, groups 1 and 2 are also strongly anti-correlated with each other and they have no significant correlation with group 3. We exploit these correlations and use PCA to reduce the dataset dimensionality to a single robust parameter, which explain a large amout of data variance (e.g., Jolliffe and Cadima, 2016).

This first (main) component of the PCA represents more than 92% of the total variance in the concentration of SiO_2, Na_2O, TiO_2, Al_2O_3, K_2O, Fe_2O_3, and MgO and is interpreted as indicative of the bulk sediment composition (Table S2). The remaining ca. 8% of the variance distributed along the other six components of the PCA, is disregarded in the following analysis. We indicate with $PCA1_{score}$ the projection of the data along the first eigenvector of the covariance matrix, which is a dimensionless variable. The $PCA1_{score}$ is strictly related to the chemical composition of the rock samples, in particular, high values of $PCA1_{score}$ indicate sediments with high concentrations of SiO_2, and Na_2O and low concentrations of Al_2O_3, K_2O, Fe_2O_3, MgO and TiO_2. Vice versa for low values of $PCA1_{score}$. A diagram of $PCA1_{score}$ vs. depth is shown in Fig. 2B together with sediment lithology ranked according to the grain size.

The concentration of SiO_2 typically indicates the amount of quartz in siliciclastic sediments, the Na_2O association is indicates the amount of plagioclase feldspar, whilst high concentrations of Al_2O_3 is often indicative of clay minerals (Ratcliffe et al., 2015). Accordinly, high/low values of $PCA1_{score}$ are indicative of sandstones/claystone respectively. Fig. 4B shows the boxplots and the frequency of occurrence of $PCA1_{score}$ in groups of specimens divided by lithologies classified in five

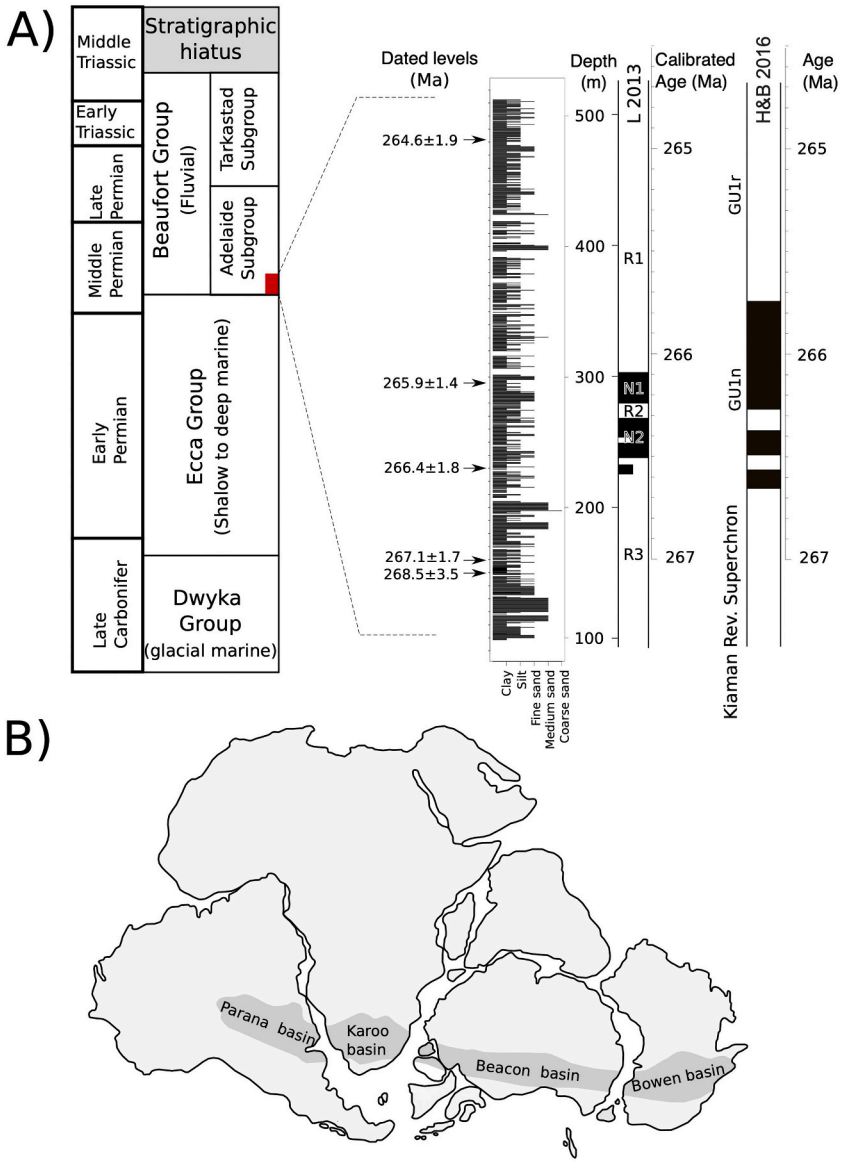

Fig. 2. A) Studied section with ranked lithology and dated levels within the stratigraphic scheme of the Karoo supergroup. On the right it is shown the comparison of the magnetostratigraphy of Ouberg Pass (Lanci et al., 2013) and calibrated age (this paper) with the Hounslow and Balabanov (2016) reference scale. The absolute age scale of the calibrated Ouberg Pass was obtained as described in the text and is independent from that of Hounslow and Balabanov (2016). B) The Karoo Basin and coeval foreland basins in the context of a paleogeographic reconstruction of Gondwana during the Late Paleozoic.

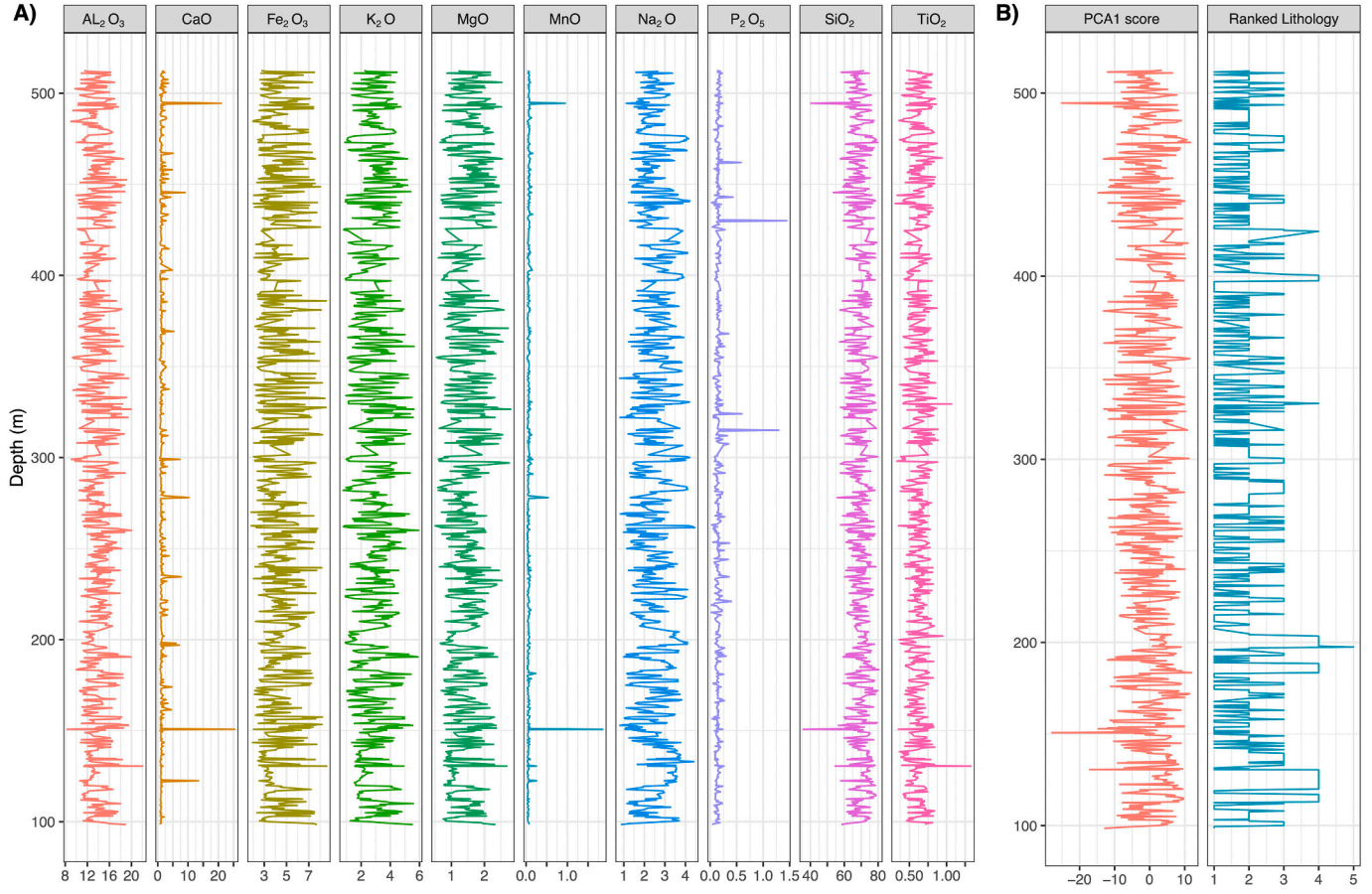

Fig. 3. A) Major element oxides concentration in the Abrahamskraal Fm. at the Ouberg Pass section expressed as percent. B) Records of $PCA1_{score}$ and Lithology ranked in 5 categories (Claystone < Siltstone < Fine Sandstone < Medium Sandstone < Coarse Sandstone).

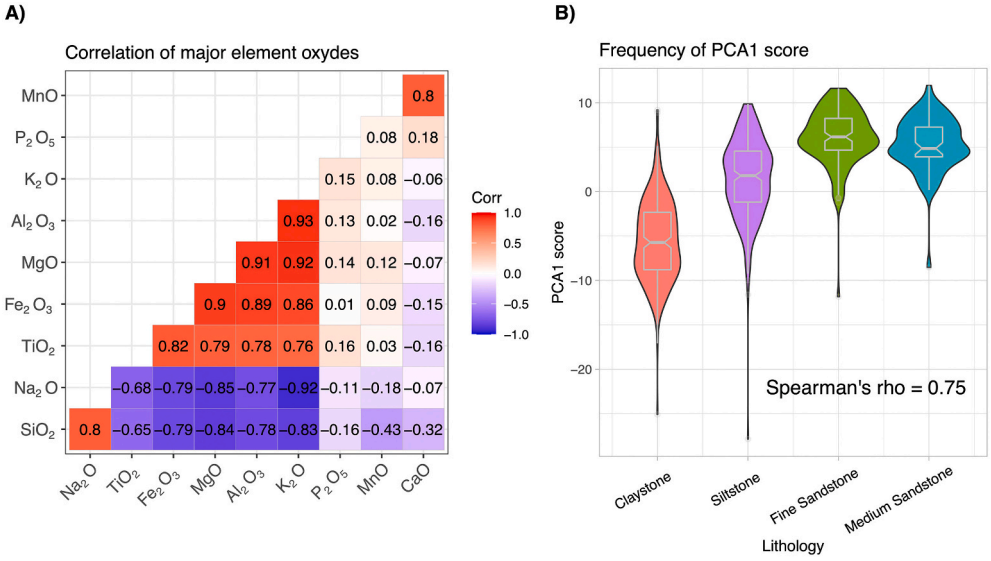

Fig. 4. A) Correlogram plot shows the Pearson's correlation coefficients between major element oxides highlighting groups of correlated oxides. B) Boxplots and violin plots of the $PCA1_{score}$ divided in groups corresponding to the main lithologies. Coarse grained sandstones have been dropped because of too few data points. Coarser lithologies are characterized by higher $PCA1_{score}$ suggesting a general interpretation of $PCA1_{score}$ in terms of lithology.

categories, from claystone to coarse sandstone. It shows that sandstones have, on average, higher values of $PCA1_{score}$, hence high concentrations of SiO_2 and Na_2O, claystones have lower values of $PCA1_{score}$, hence high concentrations of Al_2O_3, K_2O, Fe_2O_3, MgO and TiO_2, whilst siltstones have intermediate values. This visual correlation is supported by the Spearman's rank correlation computed between the ranked lithology (claystone < siltstone < fine sandstone < medium sandstone < coarse sandstone) and $PCA1_{score}$. The resulting correlation coefficient $\rho = 0.75$

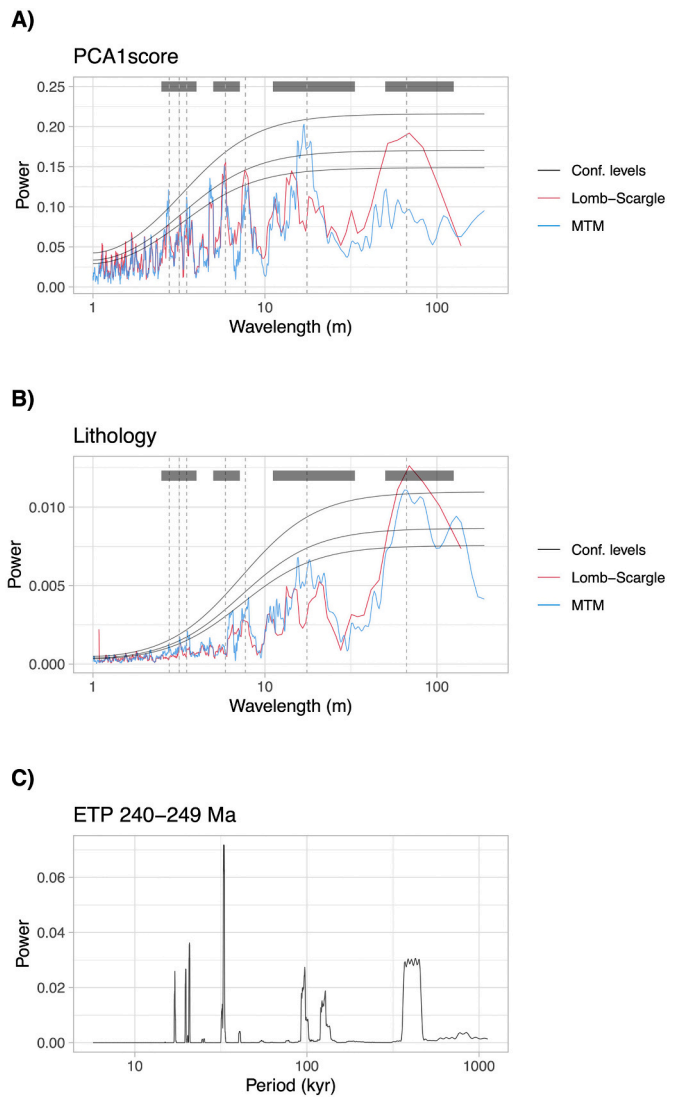

Fig. 5. Power spectra of $PCA1_{score}$ and ranked Lithology. The power spectra are estimated using the smoothed Lomb-Scargle periodogram (in red) and the MTM (in blue), the confidence levels of 90%, 95% and 99% computed for the MTM spectra are shown in black. Vertical dashed lines highlight the main spectral peaks and horizontal grey bands represent the frequency bands that were used in the band-pass filtering. Main peaks have the same wavelength of 67 m, 17.5 m, 7.7 m, 5.9 m, 3.51 m, 3.17 m and 2.70 m in both upper diagrams. The MTM power spectrum of ETP for the time interval between 240 and 249 Ma is show in the bottom panel for comparison. The period of ETP spectrum has been rescaled to the depth using the optimal sedimentation rate of 16 cm/kyr. (For interpretation of the references to colour in this figure legend, the reader is referred to the web version of this article.)

is statistically significant at the 99% confidence level confirming the interpretation of the analytical data in terms of field lithology.

4.2. Spectral analysis and astronomical tuning

The power spectra of $PCA1_{score}$ and ranked lithology are similar and show the presence of distinct frequency peaks exceeding the confidence level of 95% (Fig. 5). Statistically significant peaks that can potentially represent the record of cyclic orbital variations in the sediments of the Abrahamskraal Fm. have been identified with depth frequencies of 0.015, 0.057, 0.17, 0.28, 0.31, 0.36 cycles/m and corresponding wavelengths of 67, 17.5, 5.9, 3.5, 3.2, 2.8 m. There is a good agreement of the power spectra computed with the MTM and the smoothed Lomb-Scargle periodogram suggesting that interpolation to evenly-spaced depth intervals does not alter the spectral content of the data. It is worth noticing that the 17.5 m peak is split in the Lomb-Scargle periodograms, representative of the two components (e2/e3) of short eccentricity, and the 67 m peak is less pronounced in the MTM spectra.

The wavelet power spectra of $PCA1_{score}$ and ranked lithology are also remarkably similar (Fig. 6). Moreover, the cumulative spectra, shown in the right panels of Fig. 6, resemble closely the MTM spectra and displays peaks with approximately the same periodicities, with the limit of the lower resolution for short wavelengths in the cumulative wavelet spectra. Wavelets exhibit well-defined horizontal frequency bands and especially the spectral bands with wavelengths of 67 m and 17.5 m are relatively continuous and rectilinear, which is suggestive of a rather constant sedimentation rate through the record. Continuous frequency bands imply that hiatuses or changes in sedimentation rate, which are not unusual in a continental sedimentary record, do not have a severe effect on the periodic behaviour of the sediment composition at least at the scale considered. Shorter wavelength cyclicities are not as regular and some disturbance cannot be discounted.

We interpret the remarkable regularity and the close match in timescales with orbital forcing of the Abrahamskraal sedimentation as an indication that these sedimentary cycles are paced by allogenic, astronomically-forced climate changes. According to the first-order estimate of the sedimentation rate of 11.1 cm/kyr obtained from radiometric dating (Fig. S1), it is reasonable to interpret the major peak at the frequency of 0.057 cycles/m (or wavelength of 17.5 m) as the sedimentary expression of the short eccentricity, although e2 and e3 cannot be separated at the resolution bandwidth used for these spectra. In this interpretation, the 17.5 m wavelength periodicity corresponds to about 110 kyr (the average period of e2 and e3), hence to a sedimentation rate of about 16 cm/kyr. The higher frequency peaks agree well with the main obliquity (0.17 cycles/m) and precession peaks (0.28, 0.31 and 0.36 cycles/m). The lowest frequency peak at 0.015 cycles/m (ca. 67 m wavelength) corresponds to the long eccentricity within the uncertainty of the frequency bandwidth resolution.

To validate this interpretation and compute an optimal sedimentation rate we use the averaged spectral misfit (ASM) method of Meyers and Sageman (2007) that correlates stratigraphic periodicities to the expected astronomical periods. Results are shown in Fig. 7. As target frequencies for ASM we used the expected astronomical periods for the Middle Permian (Table S1), which were compared with the stratigraphic wavelengths of 67, 17.5 m, 5.9 m, 3.51 m, 3.17 m and 2.78 m obtained from the major peaks detected in the power spectra (Fig. 5). Given the prior constraints from the radiometric estimate, we have searched for the optimal sedimentation rate within a large interval ranging from 1 cm/kyr to 25 cm/kyr and we obtained unique ASM minimum. We take the midpoint of the ASM minimum as the optimal sedimentation rate that corresponds to ca. 16 cm/kyr, since small changes of sedimentation rates do not significantly affect the results (Fig. 7). The period (in kyr) of the main frequency peaks computed accordingly to the optimal sedimentation rate are shown in Table 1; it is worth noticing that the obliquity and precession periods, which are affected by tidal dissipation, are remarkably close to the Waltham's (2015) model and virtually identical to the 21–17-kyr described in coeheval lacustrine record of the Lucaogou Formation, China (Huang et al., 2020).

We have filtered the periodic components that we interpreted as the astronomical forcing, by applying a Gaussian band-pass frequency filters to the $PCA1_{score}$ and the lithology ranks. The group of peaks with highest frequencies of 0.28, 0.31 and 0.36 cycles/m (corresponding to ca. 3.5 to 2.7 m wavelengths), which we interpret as precessional, were isolated using a gaussian shaped bandpass filter between 0.25 and 0.4 cycles/m. For the intermediate peak at 0.17 cycles/m (ca. 5.9 m wavelength), which represents obliquity, we used band-pass frequencies between 0.14 and 0.2 cycles/m. The largest peak of power spectra with a wavelength of 17.5 m (0.057 cycles/m), which is interpreted as short eccentricity, was isolated using band-pass frequencies between 0.03 and 0.09 cycles/

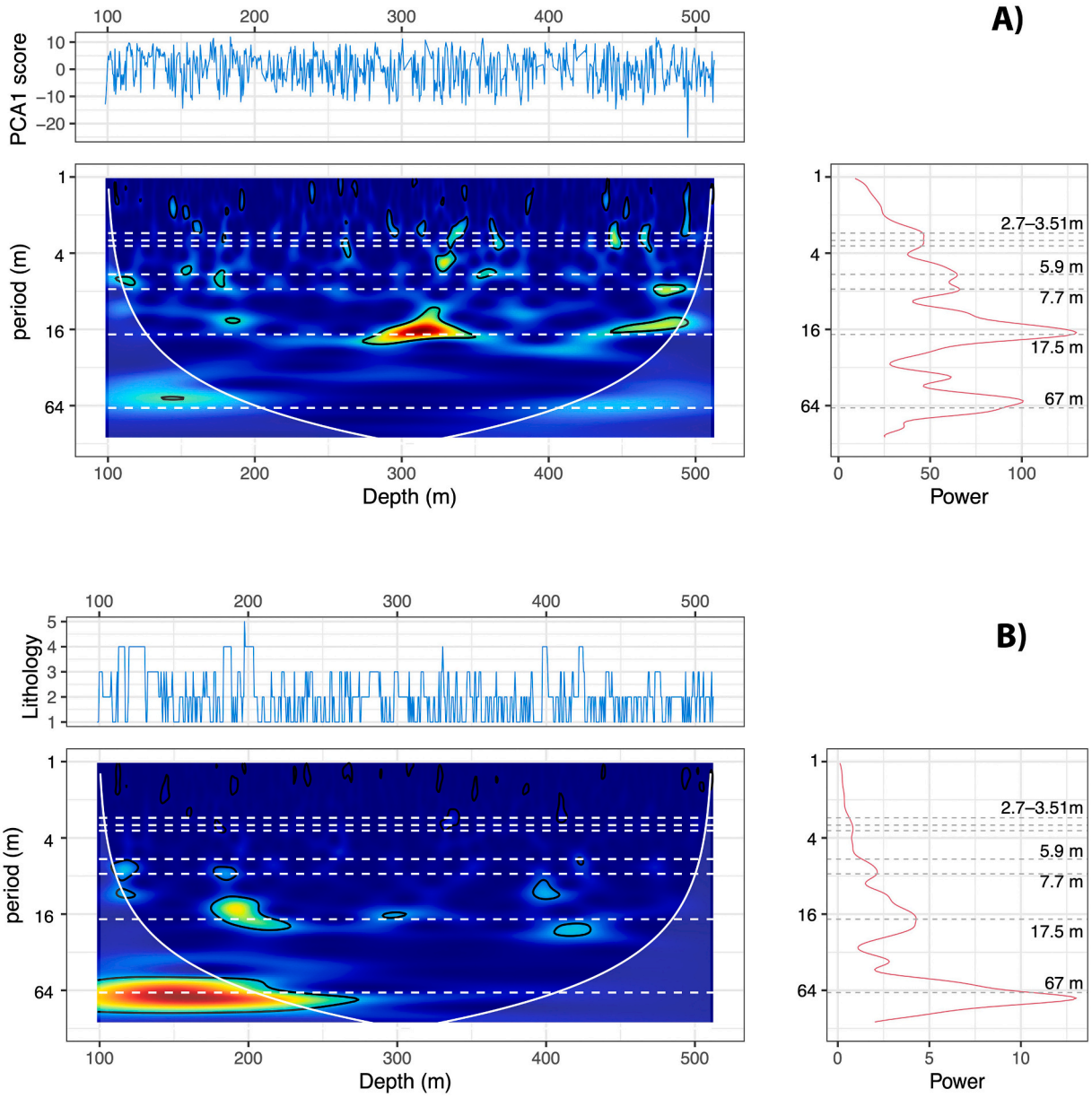

Fig. 6. Wavelet power spectra and cumulative spectra of $PCA1_{score}$ and ranked Lithology. Wavelet spectrum and confidence level were computed according to the method of Torrence and Compo (1998) using a Morlet wavelet with a characteristic frequency of seven. The 95% confidence interval is indicated by the thicker contour lines and the white line illustrates the cone of influence regions where edge effects might underestimate the amplitudes. Horizontal dashed lines identify the major periodicities found also in the MTM spectra with wavelength of 67 m, 17.5 m, 7.7 m, 5.9 m, 3.51 m, 3.17 m and 2.70 m.

m while the longest period with a wavelength of 67 m was filtered with the bandpass of 0.008–0.02 cycles/m. Band-pass frequencies are visually shown in Fig. 5 as horizontal grey bands. An inspection of the filtered signal suggests an amplitude modulation whose frequency was inferred by computing the power spectrum of the Hilbert transform (i.e., the "envelope") of filtered signal. Details of filtering, Hilbert transform and subsequent analysis can be found in the supplemental material. Results, shown in Fig. 8, highlight the presence of the significant modulations of obliquity and precession. Power spectra of instantaneous amplitudes of obliquity and precession, suggests the presence of a ca. 800 kyr period in the modulation of the obliquity as expected from astronomical solution, while a significant peak corresponding to the frequency of the short eccentricity (110 kyr), is shown by the modulation of the precession signal (Fig. S2).

Lacking a reliable astronomical solution for the Permian period, the astronomical tuning can be done either by assuming a constant sedimentation rate of 16 m/kyr or assigning each cycle in depth scale an age multiple of the averaged astronomical period. We have done this using both the band-pass filtered eccentricity and obliquity signals from the $PCA1_{score}$ and periods of 405 kyr and 110 kyr for long and short eccentricity (average of e2 and e3) and of 36.1 kyr for obliquity (Fig. 8A). Virtually identical results can be obtained using lithology ranks (Fig. 8B). The 405 kyr cyclicity is considered the most stable, hence it should generally be a preferable target for tuning. Unfortunately, in our relatively short record it is not very well espressed (Fig. 9) and it is subject to larger bandwidth uncertainty as shown in Table 1 and Fig. 7B. Cycle counting is also affected by errors due to neglecting the frequency modulation in the filtered signal, which is ignored when assuming that all cycles have exactly the same period. This effect, which has minor consequences on the age model, is highlighted in the power spectra of the tuned serie by the anomalous amplification of the peak corresponding to the tunig period (Fig. S3). In any case, the diffence observed

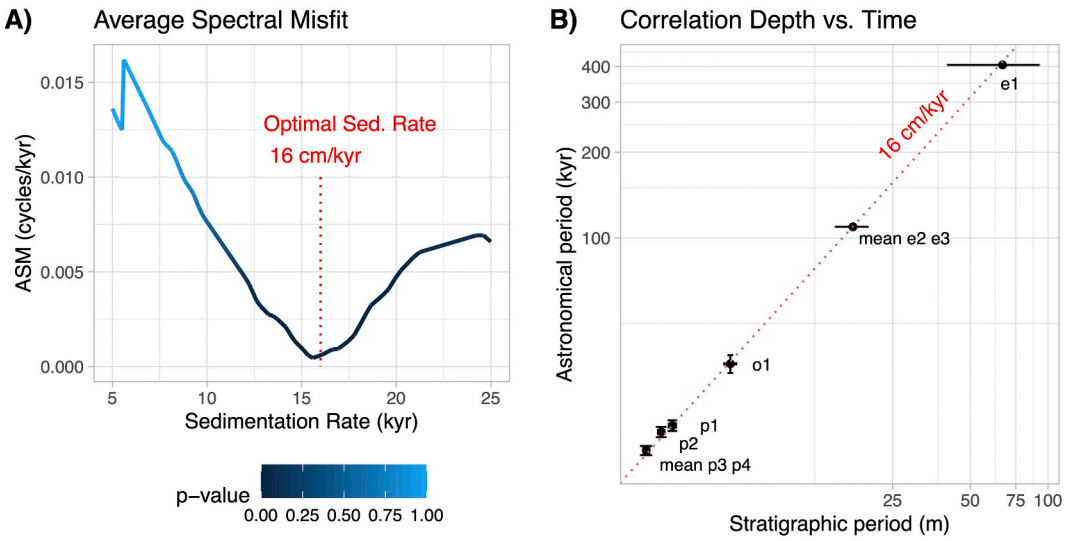

Fig. 7. a) Optimal sedimentation rate according to the average spectral misfit technique. The average spectral misfit minimum indicates an optimal sedimentation rate of 16 cm/kyr with a highly significant *p*-value <0.001. b) Comparison of orbital periods and stratigraphic wavelengths. The dashed line corresponds to the optimal sedimentation rate; errors in astronomical periods are from Waltham (2015) and the errors in the stratigraphic wavelengths correspond to the resolution bandwidth of the MTM.

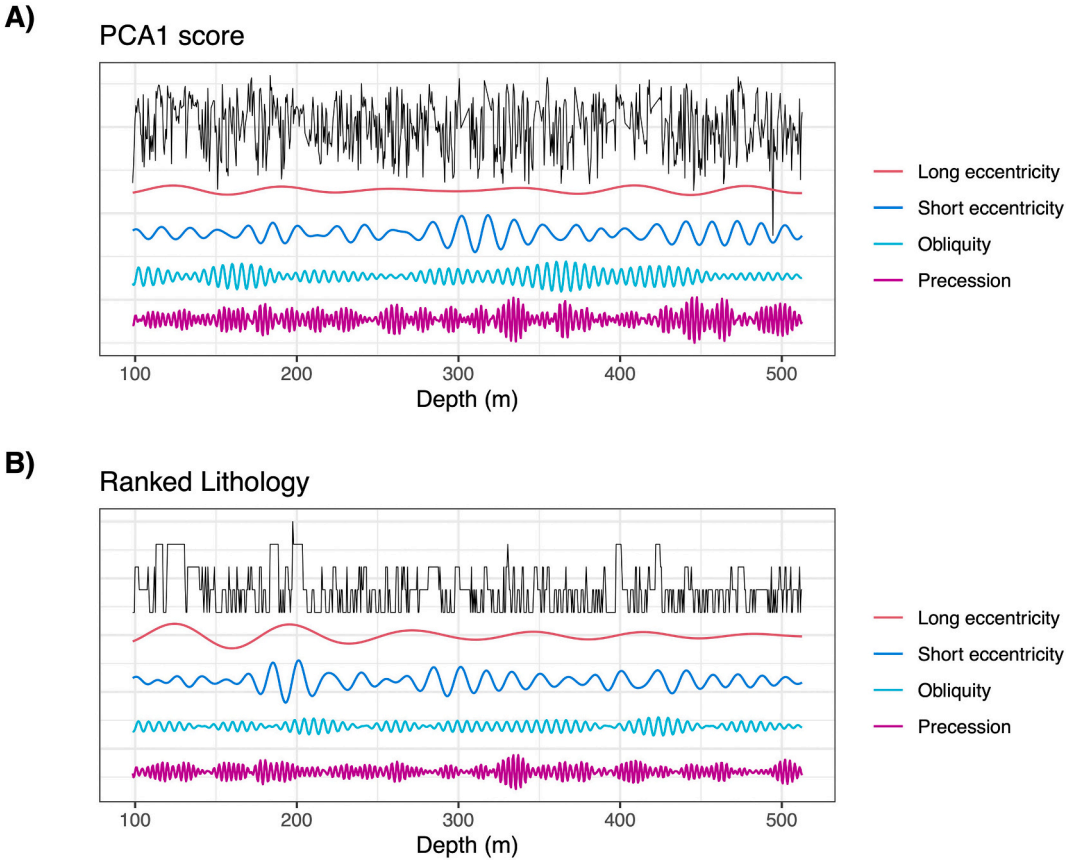

Fig. 8. Bandpass frequency filters of the $PCA1_{score}$ A) and Ranked Lithology B). Bandpass frequencies are marked as grey bands in Fig. 6. Bandpass frequencies are 0.25–0.4 cycles/m for precession, 0.14–0.2 cycles/m for obliquity, 0.03–0.09 cycles/m for short eccentricity and 0.008–0.02 cycles/m for long eccentricity.

in the age models computed by counting cycle of both short and long eccentricity, obliquity and in the simple constant sedimentation rate are rather small as shown in Fig. 9, where lines representing different models largely overlap. Since they are virtually identical for any practical purpose the simplest age model based on constant sedimentation rate (eq. 1) is taken to estimate the age of the section. The astronomically tuned sedimentation rate was combined with the radiometric dates by finding the age model that simultaneusly fits all the U/Th dates in the least-squares sense weighted by inverse of errors (σ). For the age model with constant sedimentation rate, the absolute age of the Ouberg Pass

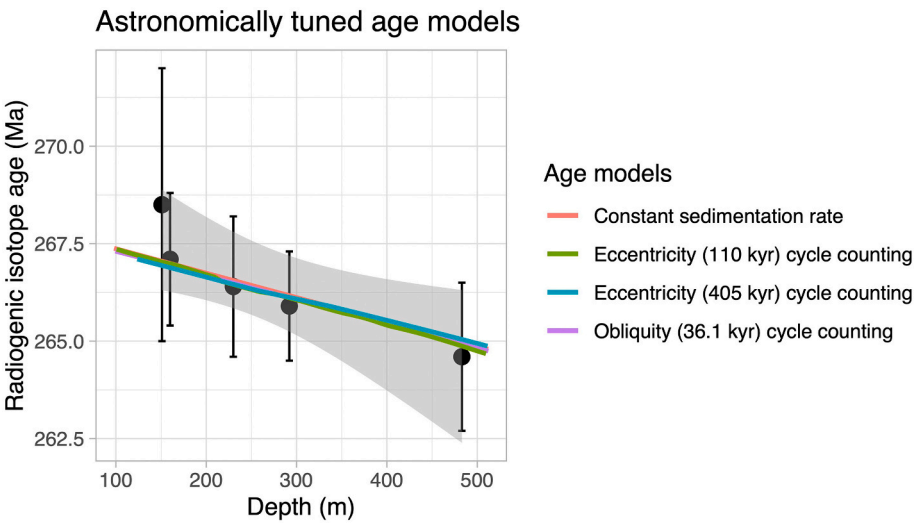

Fig. 9. Cyclostratigraphic age models for Ouberg Pass section based on the $PCA1_{score}$ record, compared to the available radiometric dates from Lanci et al. (2013). The grey band shows the 95% confidence limits of the best fit line through the dated points. Cycle counting age models are computed from $PCA1_{score}$ data.

section is given by the following expression

$$Age[Myr] = 268 \pm 0.26 - \frac{Depth[m]}{160} \quad (1)$$

where Age (in Myr) and Depth (in metres) refers to the stratigraphic depth of the Ouberg Pass measured up section. Within the errors of radiometric dates ($\sigma = 0.26$ Myr) this model provides an astronomically tuned age model with absolute ages. Details of the calculations, which were performed with R, can be found in the Supplemental Information material.

4.3. Tuning the Ouberg Pass magnetic stratigraphy

The floating age model obtained from orbital tuning of the Abrahamskraal Fm. allows a precise calibration of the duration of the Wordian magnetozones described by Lanci et al. (2013) in the Ouberg Pass section. Their absolute age can as well be assigned relying on the age model that integrates U/Pb dates (eq. 1). A simple calculation shows that the overall duration of the N1-R2-N2 magnetozone group ranges between 378 kyr and 431 kyr, depending from the ambiguity in the position of the paleomagnetic reversals resulting from the spacing between paleomagnetic specimens (Table 2). Following on the composite scale of Hounslow and Balabanov (2016) for the Permian, the N1-R2-N2 group of polarities correlates with Chron GU1n whose age of ~266 Ma coincides with the radiometric dating of the Ouberg Pass section, whilst the magnetozone R1 corresponds to the GU1r of Hounslow and Balabanov (2016) as shown in Fig. 1A. The duration of the Chron GU1r is compatible with that of the magnetozone R1, however, this must be considered a minimum duration as the upper limit of magnetozone R1 has not been identified at Ouberg Pass. The cyclostratigraphic calibration suggests that the duration of the magnetozone group N1-R2-N2, which corresponds to the Chron GU1n, is about half of that proposed by Hounslow and Balabanov (2016).

The deposition of the Ecca Group and the lowermost Abrahamskraal Fm. occurred during the Kiaman reversed superchron as confirmed by the uniform reverse polarity found in the magnetostratigraphic data from a composite, ca. 1500 m thick section of the Ecca Group in the Tanqua depocenter (Belica et al., 2017). Therefore the absolute age model for magnetozone group N1-R2-N2 provides a precise timing of the end of Kiaman superchron at 266.5 ± 0.26 Ma). Moreover, given the relatively constant sedimentation rate, based on the recurring pattern of facies associations at Ouberg Pass, we speculate that the age model of eq. (1) could be applied without major errors to the upper part of the Abrahamskraal Fm. studied in Tohver et al. (2015) if a physical correlation were established.

4.4. Origin of the astronomical forcing and Middle-Permian paleoclimate

The cyclicity observed in the $PCA1_{score}$ has a sedimentological expression that can be observed by comparing chemical composition ($PCA1_{score}$) and stratigraphic log (Fig. 10). Lithologically, cycles can be recognized as sandstone/mudstone couplets. In periods where the precession is better expressed, cycles have a thicknesses in the range of 2.7 to 3.5 m, whereas obliquity paced cycles have a thicknesses of about 6 m (Fig. 10). The lithological expression of the eccentricity cycles is found in the repetitions of the sandstone beds encountered in the logged section and in the prevalence of one phase over the other.

The identification of larger amplitude precessional cycles, independently of the completeness of the records, indicates the phase of astronomical forcing suggesting that sandstone layers occur during times of higher eccentricity. To further test this observation, we have run a spectral analysis of the filtered precessional signal aimed at detecting the FM of the precession components. We limit this analysis and the calculation of the EHA to the lowermost ~200 m of the surveyed section where no major sampling gaps are present. The EHA of the precession filter has been run using a window of 13 m, corresponding to about 4 folds the wavelength of precession cycles, as suggested by Laurin et al. (2016) and shows a neat record of FM with regularly spaced bifurcations and junctions (Fig. S4). Importantly, bifurcations/junctions in the EHA spectrum correspond to intervals of low/high variance in the precession filter demonstrating a remarkable consistency between the amplitude and the frequency modulations in the precession record of the Abrahamskraal Fm. and providing further validation to our cyclostratigraphic interpretation.

We explain the observed orbital forcing using the model of Abels et al. (2013, 2016) and the numerical simulations of Wang et al. (2020), which are based on the alluvial architecture model of Karssenberg and Bridge (2008). They show that floodplain cyclicity can be entirely produced by variations in sediment supply over water discharge (*Qs/Qw* ratio). In particular they found that alluvial stratigraphic cycle consists of two phases: 1) an avulsion phase with episodes of large-scale fluvial system reorganization characterized by rapid sedimentation due to frequent channel shifting with prevalent sands deposition that occurs during periods of increasing *Qs/Qw* and 2) an overbank phase with substantial floodplain stability where high fluvial discharge results in overspill of the trunk channels (i.e. flooding) producing crevasse splay

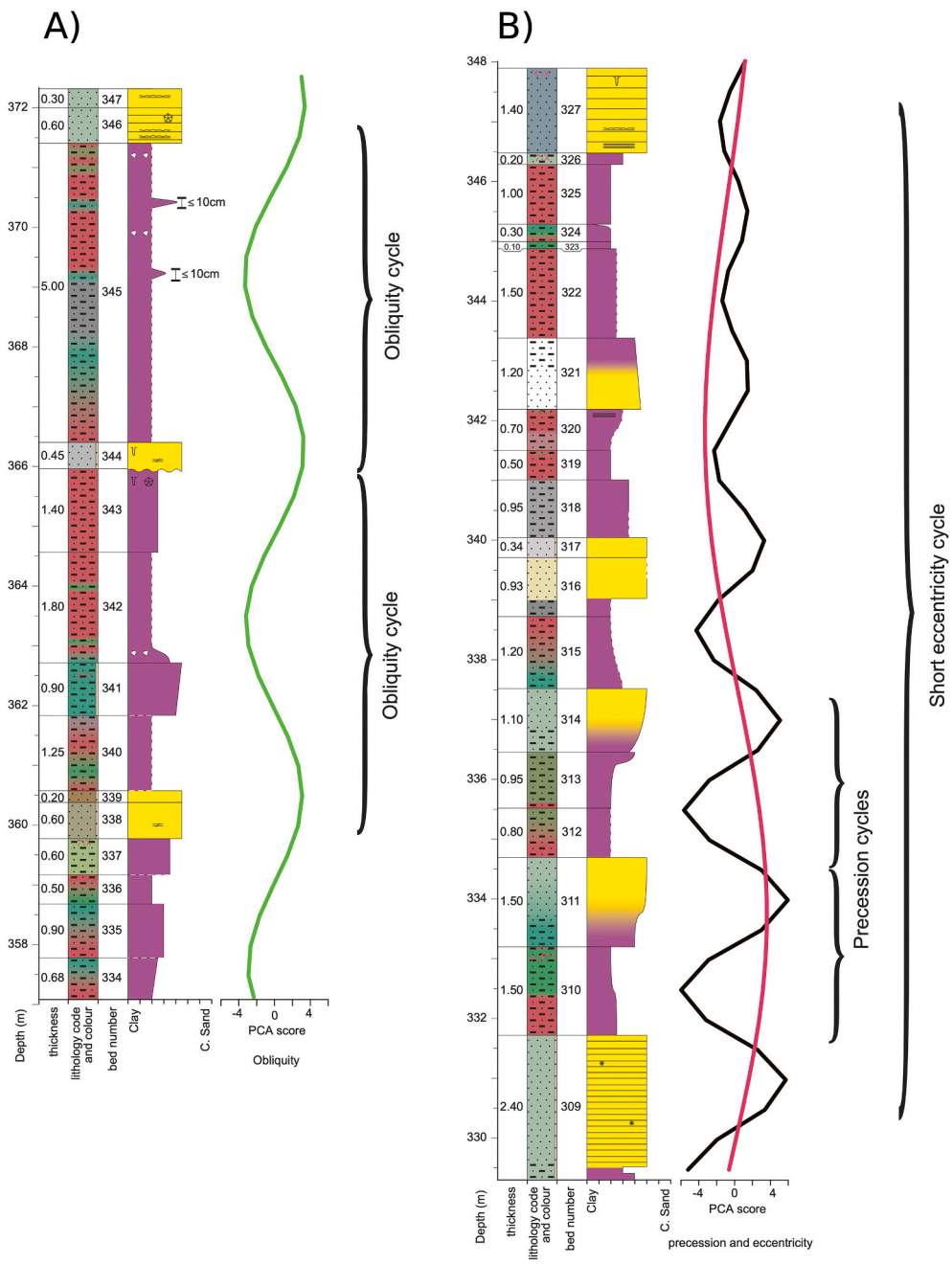

Fig. 10. Examples of the sedimentary expression of obliquity dominated A), and precession/eccentricity dominated B) orbital forcing identified by comparing the filtered $PCA1_{score}$ record with the stratigraphic log. Filter band pass parameters are 0.14–0.2 cycles/m for obliquity (green), 0.25–0.4 cycles/m for precession (black) and 0.03–0.09 cycles/m for short eccentricity (red). Most cycles in the $PCA1_{score}$ record have a clear stratigraphic correspondence. In the graphic log yellow fills denote sandstones whereas purple fills denote mudstones. (For interpretation of the references to colour in this figure legend, the reader is referred to the web version of this article.)

Table 1
Main spectral peaks, their periods assuming the optimal sedimentation rate = 16 cm/kyr) and interpretation in terms of astronomical frequencies.

Wavelength (m)	period (kyr)	Interpretation with (expected period)
67 ± 26	419 ± 162	e1 (405 kyr)
17.5 ± 2.5	109 ± 16	mean e2 and e3 (110 kyr)
5.90 ± 0.3	37 ± 2	o1 (36.1 kyr)
3.51 ± 0.11	22 ± 0.7	p1 (21.9 kyr)
3.23 ± 0.09	20 ± 0.6	p2 (20.8 kyr)
2.70 ± 0.07	17 ± 0.4	mean p3 and p4 (17.9 kyr)

Errors derive from MTM resolution bandwidth.

Table 2
Depth of paleomagnetic reversals at Ouberg Pass section in metres.

Chron	top min.	top max.	bottom min.	bottom max.
R1	525	–	300.5	305
N1	300.5	305	278	289
R2	278	289	267	268
N2	267	268	236	240

and floodplain deposition occuring during decreasing *Qs/Qw* ratio. Accordingly, low precipitation regimes coincide with avulsion times and deposition of sandy facies, whereas high precipitation regimes correspond to times of channel stability and muddy deposition over the floodplain. The precession and obliquity cycles expressed as rhythmic vertical changes of facies in the Abrahamskraal Fm. can thus be interpreted as episodes of large-scale fluvial system reorganization featured by laterally-extensive sandstone intervals and an overbank phase, controlled by changes in the hydrological cycle. Compared to the simulations of Wang et al. (2020), where during the overbank phase the vast floodplain undergoes very low sedimentation, the deposition of the

Ouberg Pass deposition appears to be dominantly aggradational even during this phase except for some minor local incision (1 m to 5 m in stratigraphic thickness) at the bases of channel belts (Wilson et al., 2014).

In the Pangea supercontinents high CO_2 levels and the paleogeographic setting favored the transition from an icehouse condition to a so-called mega-monsoon climate characterized by pronounced continentality during the Late Permian and the Triassic (Kutzbach and Gallimore, 1989; Barron and Fawcett, 1995; Winguth and Winguth, 2012). Astronomically-driven changes in regional incoming solar radiation on temperature, precipitation and associated runoff with enhanced continentality provides an influential control mechanism for climate changes in continental areas (Winguth and Winguth, 2012). In line with numerical simulation, several field observations indicate a strong signature of precession. Yet, these observations are limited to the northern hemisphere. The observation of a strong precessional signature in the Karoo basin provides a test for numerical simulations of precession-driven monsoon variability model (e.g., Winguth and Winguth, 2012) also for the southern hemisphere. In this context it is suggested that sandy interval corresponds to times of reduced seasonality and minimal monsoon regime across Gondwana, allowing the Qs/Qw ratio to increase. Minimal seasonality of the study area requires austral summer to occur in aphelion with a precession angle of 270°. For these conditions, however, the numerical simulation of precipitation predicts no relevant change in precipitation compared to maximal precession forcing (precession angle of 90°) over the Karoo basin (Winguth and Winguth, 2012). Yet, the preservation of an orbital signature in a fluvial sedimentary environment such as that of the Abrahamskraal Formation requires a large amplitude of astronomically forced environmental changes (Wang et al., 2020). All in all, therefore, the field observation from the Karoo Basin provides no validation to numerical simulation of Pangean climates for the Southern hemisphere.

5. Conclusions

The Abrahaskraal Fm. proved to be a rare case of fluvial sequence with a dominant allogenic control of sedimentation driven by astronomical cycles and the first record of Middle Permian Milankovich cyclicity in the southern hemisphere. The astronomical signature has a strong characterization with meter-scale sedimentary cycles of 67 m, 17.5 m, 5.9 m and 3.5–2.8 m representing a nearly complete spectrum of astronomical frequencies that are coherent with available radiometric dates. The periodicity of obliquity and precession, which are subject to long term variability due to tidal dissipation, are very close to the predictions made by the models of Laskar et al. (2004) and Waltham (2015) providing an experimental validation of the astronomical theory.

The floating astrochronology of the Ouberg Pass section allowed calibration of the duration of the Wordian magnetozones R1 to N2 of Lanci et al. (2013) and the integration of the floating chronology with radiometric ages improved the absolute dating of the whole section indicating an age of 266.5 ± 0.26 Ma for the end of Kiaman superchron.

Cyclic variability in sediment lithology and composition was interpreted in term of changes in hydrological regime according to the model of Abels et al. (2013, 2016) and the numerical calculations of Wang et al. (2020). Our interpretation suggests that the strong monsoonal circulation experienced by Pangea supercontinents climate (e.g., Parrish, 1993; Kutzbach and Gallimore, 1989), which resulted in extreme variability of precipitation between dry and wet periods, extended to the middle latitude (approx. 47° S) providing new constrains for paleo climate modeling.

Declaration of Competing Interest

The authors declare that they have no known competing financial interests or personal relationships that could have appeared to influence the work reported in this paper.

Acknowledgements

We would like to thank all persons involved in the Beaufort Project funded by Chevron Australia, in particular Anne Powell, A. Palfrey, T. Payenberg, J. Vermeulen, E. King, G. Hildred, D. Cole, A. Mistry, M. Yan, J, Hansma. This work was supported by Chevron Australia Pty Ltd. by the Australian Research Council (LP0991834) and by DISPEA research funds project 2019. The suggestions of two anonymous reviewers were very useful to improve the manuscript.

Appendix A. Supplementary data

Supplementary data to this article can be found online at https://doi.org/10.1016/j.palaeo.2022.110973.

References

Abels, H.A., Kraus, M.J., Gingerich, P.D., 2013. Precession-scale cyclicity in the fluvial lower Eocene Willwood Formation of the Bighorn Basin, Wyoming (USA). Sedimentology 60, 1467–1483. https://doi.org/10.1111/sed.12039.

Abels, H.A., Lauretano, V., van Yperen, A.E., Hopman, T., Zachos, J.C., Lourens, L.J., Bowen, G.J., 2016. Environmental impact and magnitude of paleosol carbonate carbon isotope excursions marking five early Eocene hyperthermals in the Bighorn Basin, Wyoming. Clim. Past 12, 1151–1163. https://doi.org/10.5194/cp-12-1151-2016.

Barron, E.J., Fawcett, P.J., 1995. The climate of Pangea: a review of climate model simulations of the Permian. In: Scholle, P.A., Peryt, T.M., Ulmer-Scholle, D.S. (Eds.), The Permian of Northern Pangea: Paleogeography, Paleoclimates, Stratigraphy, vol.1. Springer-Verlag, New York, pp. 37–52.

Belica, M.E., Tohver, E., Poyatos-Moré, M., Flint, S., Parra-Avila, L.A., Lanci, L., Denyszyn, S., Pisarevsky, S.A., 2017. Refining the chronostratigraphy of the Karoo Basin, South Africa: magnetostratigraphic constraints support an early permian age for the Ecca Group. Geophys. J. Int. 211 (3), 1354–1374. https://doi.org/10.1093/gji/ggx344.

Bordy, E.M., Paiva, F., 2021. Stratigraphic architecture of the Karoo River channels at the end-capitanian. Front. Earth Sci. 8, 521766 https://doi.org/10.3389/feart.2020.521766.

Catuneanu, O., Wopfner, H., Eriksson, P.G., Cairncross, B., Rubidge, B.S., Smith, R.M.H., Hancox, P.J., 2005. The Karoo Basins of South-Central Africa. J. Afr. Earth Sci. https://doi.org/10.1016/j.jafrearsci.2005.07.007.

Cong, F., Zhu, F., Cai, Z., Chen, H., Li, J., Wang, Y., Wang, L., 2019. Orbitally forced glacio-eustatic origin of third-order sequences and parasequences in the Middle Permian Maokou Formation, South China. Mar. Pet. Geol. 99, 237–251.

Day, M.O., Ramezani, J., Frazer, R.E., Rubidge, B.S., 2022. U-Pb zircon age constraints on the vertebrate assemblages and palaeomagnetic record of the Guadalupian Abrahamskraal Formation, Karoo Basin, South Africa. J. Afr. Earth Sci. 186, 104435 https://doi.org/10.1016/j.jafrearsci.2021.104435.

Fang, Qiang, Huaichun, Wu, Hinnov, Linda A., et al., 2015. Geologic evidence for chaotic behavior of the planets and its constraints on the third-order eustatic sequences at the end of the Late Paleozoic Ice Age. Palaeogeogr. Palaeoclimatol. Palaeoecol. 440, 848–859.

Fang, Qiang, Huaichun, Wu, Hinnov, Linda A., et al., 2017. Astronomical cycles of Middle Permian Maokou Formation in South China and their implications for sequence stratigraphy and paleoclimate. Palaeogeogr. Palaeoclimatol. Palaeoecol. 474, 130–139.

Galeotti, S., Moretti, M., Sabatino, N., Sprovieri, M., Ceccatelli, M., Francescone, F., Lanci, L., Lauretano, V., Monechi, S., 2017. Cyclochronology of the early eocene carbon isotope record from a composite contessa road-bottaccione section (Gubbio, Central Italy). Newsl. Stratigr. 50 (3), 231–244. https://doi.org/10.1127/nos/2017/0347.

Gouhier, T.C., Grinsted, A., Simko, V., 2021. R package biwavelet: Conduct Univariate and Bivariate Wavelet Analyses (Version 0.20.21). https://github.com/tgouhier/biwavelet.

Gulliford, A.R., Flint, S.S., Hodgson, D.M., 2014. Testing applicability of models of distributive fluvial systems or trunk Rivers in ephemeral systems: reconstructing 3-D fluvial architecture in the Beaufort Group. South Afr. J. Sed. Res. 84 (12), 1147–1169. https://doi.org/10.2110/jsr.2014.88.

Hounslow, M.W., Balabanov, Yuri P., 2016. A geomagnetic polarity timescale for the Permian, calibrated to stage boundaries. Geol. Soc. Spec. Publ. https://doi.org/10.1144/SP450.8.

Huang, H., Gao, Y., Jones, M.M., Tao, H., Carroll, A.R., Ibarra, D.E., Wu, H., Wang, C., 2020. Astronomical forcing of middle permian terrestrial climate recorded in a large Paleolake in Northwestern China. Palaeogeogr. Palaeoclimatol. Palaeoecol. 550 (109735) https://doi.org/10.1016/j.palaeo.2020.109735.

Jarvis, I., Jarvis, K.E., 1992a. Inductively coupled plasma-atomic emission spectrometry in exploration geochemistry. In: Hall, G.E.M., Vaughlin, B. (Eds.), Analytical Methods in Geochemical Exploration, pp. 139–200. Journal of Geochemical Exploration, special issue 44.

Jarvis, I., Jarvis, K.E., 1992b. Plasma spectrometry in earth sciences: techniques, applications and future trends. In: Jarvis, I., Jarvis, K.E. (Eds.), Plasma Spectrometry in Earth Sciences, Chemical Geology, 95, pp. 1–33 (special issue).

Johnson, M.R., Van Vuuren, C.J., Visser, J.N.J., Cole, D.I., Wickens, H. de V., Christie, A. D.M., Roberts, D.L., 1997. The foreland Karoo Basin, South Africa. In: Hsü, K.J. (Ed.), African Basins—Sedimentary Basins of the World. Elsevier, Amsterdam, pp. 269–317.

Jolliffe, I.T., Cadima, J., 2016. Principal component analysis: a review and recent developments. Philos. Trans. A Math. Phys. Eng. Sci. 374 (2065), 20150202. https://doi.org/10.1098/rsta.2015.0202.

Karssenberg, D., Bridge, J.S., 2008. A three-dimensional numerical model of sediment transport, erosion and deposition within a network of channel belts, floodplain and hill slope: extrinsic and intrinsic controls on floodplain dynamics and alluvial architecture. Sedimentology 55, 1717–1745. https://doi.org/10.1111/j.1365-3091.2008.00965.x.

Keyser, A.W., 1966. Some indications of an arid climate during deposition of the Beaufort Series. Ann. Geol. Survey S. Afr. 5, 77–80.

Kutzbach, J.E., Gallimore, R.G., 1989. Pangaean climates: Megamonsoons of the megacontinent. J. Geophys. Res. 94, 3341–3357.

Lanci, L., Tohver, E., Wilson, A., Flint, S., 2013. Upper permian magnetic stratigraphy of the lower Beaufort Group, Karoo Basin. Earth Planet. Sci. Lett. https://doi.org/10.1016/j.epsl.2013.05.017.

Laskar, J., Robutel, P., Joutel, F., Gastineau, M., Correia, A.C.M., Levrard, B., 2004. A long-term numerical solution for the insolation quantities of the earth. Astron. Astrophys. 428.

Laurin, J., Meyers, S.R., Galeotti, S., Lanci, L., 2016. Frequency modulation reveals the phasing of orbital eccentricity during Cretaceous Oceanic Anoxic Event II and the Eocene hyperthermals. Earth Planet. Sci. Lett. 442, 143–156.

Liu, Y., San Liang, X., Weisberg, R.H., 2007. Rectification of the bias in the wavelet power spectrum. J. Atmos. Ocean. Technol. 24, 2093–2102.

Lomb, N.R., 1976. Least-squares frequency analysis of unequally spaced data. Astrophys. Space Sci. 39, 447–462.

Mann, M.E., Lees, J.M., 1996. Robust estimation of background noise and signal detection in climatic time series. Clim. Chang. 33, 409–445. https://doi.org/10.1007/BF00142586.

McKay, M.P., Weislogel, A.L., Fildani, A., Brunt, R.L., Hodgson, D.M., Flint, S.S., 2015. U-PB zircon tuff geochronology from the Karoo Basin, South Africa: implications of zircon recycling on stratigraphic age controls. Int. Geol. Rev. 57 (4), 393–410. https://doi.org/10.1080/00206814.2015.1008592.

Meyers, S.R., 2012. Seeing red in cyclic stratigraphy: spectral noise estimation for astrochronology. Paleoceanography 27, PA3228. https://doi.org/10.1029/2012PA002307.

Meyers, S.R., 2014. Astrochron: An R Package for Astrochronology. https://Cran.r-Project.Org/Web/Packages/Astrochron/Index.Html.

Meyers, S.R., Sageman, B.B., 2007. Quantification of deep-time orbital forcing by average spectral misfit. Am. J. Sci. https://doi.org/10.2475/05.2007.01.

Meyers, S.R., Sageman, B.B., Hinnov, L.A., 2001. Integrated quantitative stratig- raphy of the Cenomanian–Turonian Bridge Creek Limestone Member using evolutive harmonic analysis and stratigraphic modeling. J. Sediment. Res. 71, 628–644.

Parrish, J.T., 1993. Climate of the Supercontinent Pangea. J. Geol. 10, 215–233.

R Core Team, 2015. R: A Language and Environment for Statistical Computing. R Foundation for Statistical Computing, Vienna, Austria. http://www.R-project.org/.

Ratcliffe, K.T., Wilson, A., Payenberg, T., Rittersbacher, A., Hildred, G.V., Flint, S.S., 2015. Ground truthing chemostratigraphic correlations in fluvial systems. AAPG Bull. https://doi.org/10.1306/06051413120.

Rial, J.A., 1999. Pacemaking the ice ages by frequency modulation of Earth's orbital eccentricity. Science 285, 564–568.

Rossouw, P.J., De Villers, J., 1953. The Geology of the Merweville Area, Cape Province: An Explanation of Sheet 198 (Merweville). Geological Survey of South Africa, Pretoria, p. 80.

Scargle, J.D., 1982. Studies in astronomical time series. II. Statistical aspects of spectral analysis of unevenly spaced data. The Astrophysical Journal 302: 757–763. Palaeogeogr. Palaeoclimatol. Palaeoecol. https://doi.org/10.1016/j.palaeo.2006.03.059.

Smith, R.M.H., 1990. A review of the stratigraphy and sedimentary environments of the Karoo basin of South Africa. J. Afr. Earth Sci. 10, 117–137.

Stavrakis, N., 1980. Sedimentation of the Katberg sandstone and adjacent formations in the South-Eastern Karoo Basin. Trans. Geol. Soc. S. Afr. 83, 361–374.

Tankard, A.J., Jackson, M.P.A., Eriksson, K.A., Hobday, D.K., Hunter, D.R., Minter, W.E. L., 1982. Crustal Evolution of Southern Africa: 3.8 Billion Years of Earth History. Springer-Verlag, Berlin, p. 523p.

Tankard, A., Welsink, H., Aukes, P., Newton, R., Stettler, E., 2009. Tectonic evolution of the Cape and Karoo basins of South Africa. Mar. Pet. Geol. 26, 1379–1412.

Thomson, D.J., 1982. Spectrum estimation and harmonic analysis. Proc. IEEE 70, 1055–1096. https://doi.org/10.1109/PROC.1982.12433.

Tohver, E., Lanci, L., Wilson, A., Hansma, J., Flint, S., 2015. Magnetostratigraphic constraints on the age of the lower Beaufort Group, Western Karoo Basin, South Africa, and a critical analysis of existing U-Pb geochronological data. Geochem. Geophys. Geosyst. https://doi.org/10.1002/2015GC005930.

Torrence, C., Compo, G.P., 1998. A practical guide to wavelet analysis. Bull. Am. Meteorol. Soc. 79, 61–78.

Visser, J.N.J., 1991a. Geography and climatology of the Late Carboniferous to Jurassic Karoo Basin in South-Western Gondwana. Ann. S. Afr. Mus. 99, 415–431.

Visser, J.N.J., 1991b. The paleoclimatic setting of the Late Paleozoic marine ice sheet in the Karoo Basin of Southern Africa. In: Anderson, J.B., Ashley, G.M. (Eds.), Glacial Marine Sedimentation: Paleoclimatic Significance, Geological Society of America Special Paper, vol. 261, pp. 181–189.

Visser, J.N.J., Dukas, B.A., 1979. Upward fining fluviatile megacycles in the Beaufort Group north of Graaff Reinet, Cape Province. Trans. Geol. Soc. S. Afr. 82, 149–154.

Waltham, D., 2015. Milankovitch period uncertainties and their impact on cyclostratigraphy. J. Sediment. Res. 85, 990–998. https://doi.org/10.2110/jsr.2015.66.

Wang, Y., Storms, J.E.A., Martinius, A.W., Karssenberg, D., Abels, H.A., 2020. Evaluating alluvial stratigraphic response to cyclic and non-cyclic upstream forcing through process-based alluvial architecture modelling. Basin Res. 2021 (33), 48–65. https://doi.org/10.1111/bre.12454.

Wilson, A., Flint, S., Payenberg, T., Tohver, E., Lanci, L., 2014. Architectural styles and sedimentology of the Fluvial Lower Beaufort Group, Karoo Basin, South Africa. J. Sediment. Res. https://doi.org/10.2110/jsr.2014.28.

Winguth, A., Winguth, C., 2012. Precession-driven monsoon variability at the Permian–Triassic Implications for anoxia and the mass extinction. Glob. Planet. Chang. https://doi.org/10.1016/j.gloplacha.2012.06.006.

Wu, H., Zhang, S., Hinnov, L.A., Jiang, G., Qi. Feng, H. Li and T. Yang., 2013. Time-calibrated milankovitch cycles for the late permian. Nat. Commun. 4, 1–8. https://doi.org/10.1038/ncomms3452.

Yao, X., Hinnov, L.A., 2019. Advances in characterizing the cyclostratigraphy of binary chert-mudstone lithologic successions, Permian (Roadian-lower Capitanian), Chaohu, Lower Yangtze, South China. Palaeogeogr. Palaeoclimatol. Palaeoecol. 528, 258–271.

Yao, X., Zhou, Y., Hinnov, L.A., 2015. Astronomical forcing of a Middle Permian chert sequence in Chaohu, South China. Earth Planet. Sci. Lett. 422, 206–221.